

Technical Note

# Mapping Vulnerable Urban Areas Affected by Slow-Moving Landslides Using Sentinel-1 InSAR Data

Marta Béjar-Pizarro <sup>1,\*</sup> , Davide Notti <sup>2</sup>, Rosa M. Mateos <sup>1,3</sup>, Pablo Ezquerro <sup>1</sup>, Giuseppe Centolanza <sup>4</sup>, Gerardo Herrera <sup>1,5</sup> , Guadalupe Bru <sup>6</sup>, Margarita Sanabria <sup>1</sup>, Lorenzo Solari <sup>7</sup> , Javier Duro <sup>4</sup> and José Fernández <sup>6</sup>

<sup>1</sup> Geohazards InSAR Laboratory and Modeling Group (InSARlab), Geoscience Research Department, Geological Survey of Spain (IGME), Alenza 1, 28003 Madrid, Spain; rm.mateos@igme.es (R.M.M.); p.ezquerro@igme.es (P.E.); g.herrera@igme.es (G.H.); m.sanabria@igme.es (M.S.)

<sup>2</sup> National Research Council of Italy, Research Institute for Geo-Hydrological Protection (CNR-IRPI), Strada delle Cacce 73, 10135 Torino, Italy; davide.notti@irpi.cnr.it

<sup>3</sup> Geological Survey of Spain (IGME), Urb. Alcázar del Genil, 4-Edif. Bajo, 18006 Granada, Spain

<sup>4</sup> DARES TECHNOLOGY, Esteve Terradas, 1, Edif. RDIT, Parc UPC-PMT, 08860 Castelldefels, Barcelona, Spain; gcentolanza@dares.tech (G.C.); jduro@dares.tech (J.D.)

<sup>5</sup> EuroGeoSurveys: Earth Observation and Geohazards Expert Group (EOEG), 36-38, Rue Joseph II, 1000 Brussels, Belgium

<sup>6</sup> Institute of Geosciences (CSIC, UCM), Facultad C. Matemáticas, 28040 Madrid, Spain; gbrucruz@gmail.com (G.B.); jft@mat.ucm.es (J.F.)

<sup>7</sup> Earth Sciences Department, University of Firenze, Via La Pira 4, 50121 Florence, Italy; lorenzo.solari@unifi.it

\* Correspondence: m.bejar@igme.es; Tel.: +34-91-349-5804

Received: 23 July 2017; Accepted: 18 August 2017; Published: 23 August 2017

**Abstract:** Landslides are widespread natural hazards that generate considerable damage and economic losses worldwide. Detecting terrain movements caused by these phenomena and characterizing affected urban areas is critical to reduce their impact. Here we present a fast and simple methodology to create maps of vulnerable buildings affected by slow-moving landslides, based on two parameters: (1) the deformation rate associated to each building, measured from Sentinel-1 SAR data, and (2) the building damage generated by the landslide movement and recorded during a field campaign. We apply this method to Arcos de la Frontera, a monumental town in South Spain affected by a slow-moving landslide that has caused severe damage to buildings, forcing the evacuation of some of them. Our results show that maximum deformation rates of 4 cm/year in the line-of-sight (LOS) of the satellite, affects La Verbena, a newly-developed area, and displacements are mostly horizontal, as expected for a planar-landslide. Our building damage assessment reveals that most of the building blocks in La Verbena present moderate to severe damages. According to our vulnerability scale, 93% of the building blocks analysed present high vulnerability and, thus, should be the focus of more in-depth local studies to evaluate the serviceability of buildings, prior to adopting the necessary mitigation measures to reduce or cope with the negative consequences of this landslide. This methodology can be applied to slow-moving landslides worldwide thanks to the global availability of Sentinel-1 SAR data.

**Keywords:** landslides; InSAR; Sentinel-1; building damages

## 1. Introduction

Landslides affect mountainous regions worldwide, causing a large number of human fatalities and large economic losses [1,2]. Increasing urbanization and climate change will intensify this problem

in future years [3]. In order to reduce losses and damages, identification and mapping of vulnerable populated areas exposed to landslides are particularly critical.

The term landslide refers to the movement of a mass of rock, earth, or debris down a slope [4] including different processes, such as rockfalls, debris flows, or landslides. When these movements occur slowly, their evolution can be monitored and evaluated in early stages (e.g., [5,6]), which allows the implementation of mitigation measures to minimize their negative consequences (e.g., [7]).

Satellite-based Earth observation (EO) data have become one of the most powerful tools for landslide monitoring in the last 20 years [8]. These techniques include the use of optical satellite imagery [9–11], the use of amplitude-based SAR techniques for fast-moving landslides monitoring (up to tens of meters, e.g., [12,13]), and the use of phase-based SAR techniques for slow-moving landslides monitoring (less than a few cm/month, e.g., [5,14–17]). The latter, referred to as satellite synthetic aperture radar interferometry (InSAR), measures the changes in the satellite-to-ground distance between two or more image acquisitions [18] and thus can be used to detect ground deformation associated to slow-moving landslides. InSAR techniques have been used not only to map and characterize the actively-deforming slopes and the different mechanisms involved (e.g., [14,19,20]) but also to characterize building deformation on urban areas affected by landslides (e.g., [21,22]).

Previous works have mostly combined InSAR-derived deformation and building-recorded damage to improve landslide mapping in urban areas [20,23], or to better understand their behaviour during pre- and post-emergency management phases [22,24,25]. Other authors have combined InSAR and building information to estimate the potential damage that could be produced in individual buildings [21,26,27].

Here we present a fast and simple methodology to create a map of vulnerable buildings in an urban area affected by an active landslide, based on two parameters: (1) the deformation rate associated to each building, measured from Sentinel-1 SAR data, and (2) the damages recorded in the buildings following the classification proposed by Cooper [28]. We begin by describing the study area and the main characteristics of the Arcos de la Frontera landslide (Section 2). After outlining the materials and methods used in Section 3, we present the results from the InSAR analysis, the eastward and vertical components of the deformation field, the component of the movement parallel to the maximum slope direction, the classification of building damage and the vulnerable buildings map in Section 4. In Section 5, we examine the relationship between ground deformation and local geomorphology and analyse the correlation between damage and deformation in building blocks. Finally, we discuss the potential and limits of the vulnerable buildings map and suggest future research directions.

## 2. Study Area

Arcos de la Frontera is a village located in the northern part of the province of Cádiz (Southern Spain) in the mountainous region of the Cádiz Range. With a population around 30,000 people, Arcos de la Frontera is divided between the old town (founded in the 11th century), located on top of a rocky hill, and the newer town (built during the second half of the 20th century) extended on the lower slopes of the ridge, and on the right bank of the river Guadalete.

From a geological perspective, Arcos de la Frontera is located within the geological domain of the Guadalquivir Basin [29], and the town is settled on marine sediments, Miocene in Age. While the old town is setting on a rocky substrate composed of sandstone, the new town has extended over soft sediments: marine marls and silts, which display an expansive behaviour [30]. This soft material, named the Guadalquivir Blue Marls Formation, undergoes serious landslide problems in the region, generating multiple damages through the entire Guadalquivir Basin [31,32].

Most of the natural slopes located on the right bank of the River Guadalete, where the Guadalquivir Blue Marls Formation outcrops, are affected by landslides. In fact, these areas were avoided by the ancient settlers because of their intense slope dynamics [33]. On the western part of the old town, the urban development has progressively occupied the head of the landslides. Most of the landslides are retrogressive, complex earthflow-earth slides; the displaced material, initially broken

by planar slide movements, subsequently begins to flow. Due to the river erosion, the lower part of the slopes failed firstly and, later, new earthflows-earth slides were formed by retrogressive failures occurring progressively further upslope. The slope where the new town is located ( $\sim 17^\circ$  inclination) is on the outside bend of a meander, where erosion is more important. The Tablellina water channel, which flows parallel to the river in the lower part of the slope (Figure 1b), is currently distorted and broken into many parts, and most of the pathways along the slope are affected by numerous cracks (Figure 1d). Figure 1b shows the entire extension of the complex landslide, composed of several coalescent bodies. The landslide is 925 m in length and 950 m in width. Based on previous reports [34], the terrain displaces mainly along a planar surface of rupture and the failure surface could be at an average depth of 10 m. Currently, the crown of the landslide is located in the contact boundary between the blue marls and the sandstones.

The urban development of the new town started in the 1970s, and buildings have progressively occupied the head of the slide (Supplementary Figure S1). At the beginning of the 21st century, the housing development named “La Verbena” was built. Damage (cracks, open fractures, distorted windows, etc.) started to appear in 2006. At the time of writing, 22 families have already been evacuated (building D1 in Figure 1c) and there is a great social alarm in the town. This case is currently subject to judicial proceedings and it is of great interest for the media [35,36].

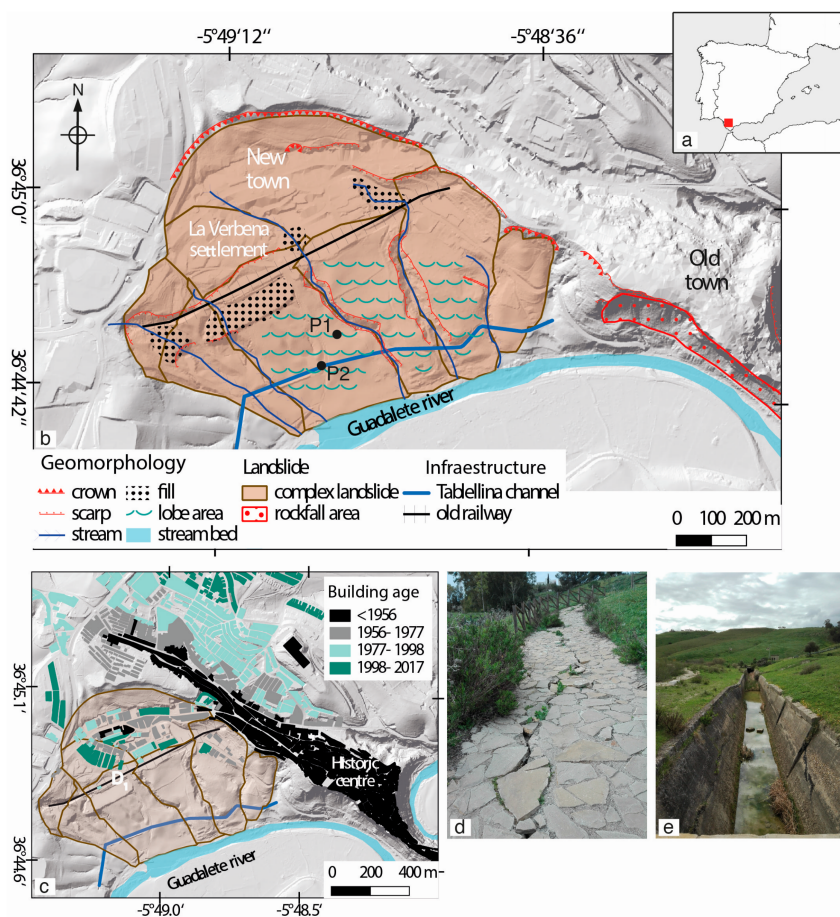


**Figure 1.** (a) Location of the study area (red rectangle) in Southern Spain; (b) map of the Arcos de la Frontera complex landslide with the main geomorphological features indicated. Labels P1 and P2 indicate the location of pictures in (d) and (e), respectively; (c) Age of building construction (from [37]). D1 indicates the position of the building block evacuated in 2009; (d) cracks in one of the pathway along the slope; and (e) cracks along the Tablellina water channel.

### 3. Materials and Methods

#### 3.1. InSAR Data

Ground deformation over the study area was measured using ascending and descending Sentinel-1A (S-1A) wide-swath SAR data. Thirty-nine S-1A images acquired from ascending track 147 (February 2015–July 2016) and forty images from descending track 154 (March 2015–July 2016) were processed using the coherent pixel technique (CPT) developed by the Remote Sensing Laboratory (RSLab) at Universitat Politècnica de Catalunya (UPC) [38–40]. The CPT interferometric chain is divided into two main blocks:

- **Prisar.** This part refers to the co-registration of SAR images and generation of interferograms, coherence maps, and differential phase matrices. The Terrain Observation by Progressive Scans (TOPS) acquisition mode of Sentinel-1 data requires an improved co-registration method [41]. Typically, it is proven that images acquired by standard mode (or stripmap) have to be aligned with an accuracy of less than 0.1 pixel to have no impact on the phase quality. This parameter is stronger (less than a few thousandths of a pixel) for the TOPS acquisition mode of S-1. The whole process to correctly co-register a slave Single Look Complex (SLC) image against the master SLC image, can be summarized in the following steps: (1) Deramping of the slave image to remove the azimuth quadratic phase term; (2) Geometric offset estimation and application; (3) Estimation of a constant offset through amplitude correlation; (4) Enhanced spectral diversity (ESD) to correct a residual offset; (5) Reramping. After co-registration, 315 and 273 multi-looked interferograms using the ascending and descending dataset, respectively, were generated, with a spatial resolution of  $40 \times 40$  m. The topographic phase contribution was removed using a 25 m digital elevation model produced by the Spanish Geographical Survey (IGN).
- **Subsoft.** This part corresponds to the advanced DInSAR algorithm and consists of four main parts: (1) Pixel selection of persistent scatterers (PS) and distributed scatterers (DS) based on the coherence of pixels; (2) Estimation of the main component of displacement and the point height; (3) Estimation and removal of atmospheric artefacts and retrieval of the temporal evolution of the deformation, also called non-linear deformation; (4) Geocoding and projection of the results.

The processing of SAR data from the ascending track, covering an area of  $160 \text{ km}^2$ , produced 4010 coherent pixels, while the processing of descending track data, covering an area of  $120 \text{ km}^2$ , produced 4778 coherent pixels. In both cases, the coherent pixels were mainly concentrated over urban areas. We used  $\pm 0.4 \text{ cm/year}$  as the stability threshold based on the standard deviation values estimated for all the PS and DS in a stable area.

Figure 2 presents the complete procedure, from SAR data to vulnerable building maps, in a flow diagram.

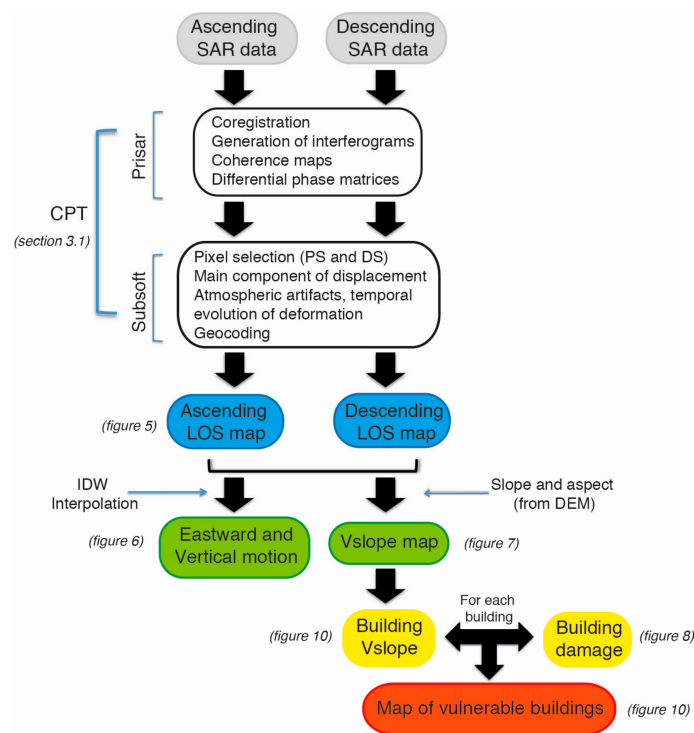


**Figure 2.** Flow diagram showing the main steps of the proposed procedure.

### 3.2. Horizontal and Vertical Deformation

Since the deformation field is obtained in two different viewing geometries (ascending and descending passes), we can obtain the 2-D deformation field (eastward and vertical motion) assuming that the north component is negligible [42,43]. Note that although the general movement in the Arcos de la Frontera landslide is NNW-SSE [44], the slope in the La Verbena settlement is oriented N110°E and, thus, locally, the movement of this area is mainly eastward.

The displacement rates along the satellite line-of-sight ( $vLOS$ ) from ascending and descending datasets were interpolated using the inverse distance weighted (IDW) method (with power 1, search radius 100 m, and three points minimum). The interpolated ascending ( $vLOS_a$ ) and descending ( $vLOS_d$ ) velocities, with  $5 \times 5$  m spatial resolution, were then used to calculate the eastward (1) and vertical (2) components of the velocity, using the raster calculator tool of the open source software Quantum GIS.

$$V_{eastward} = \frac{\left( \left( \frac{vLOS_d}{H_d} \right) - \left( \frac{vLOS_a}{H_a} \right) \right)}{\left( \frac{E_d}{H_d} - \frac{E_a}{H_a} \right)} \quad (1)$$

$$V_{vertical} = \frac{\left( \left( \frac{vLOS_d}{E_d} \right) - \left( \frac{vLOS_a}{E_a} \right) \right)}{\left( \frac{H_d}{E_d} - \frac{H_a}{E_a} \right)} \quad (2)$$

where  $H_a$ ,  $H_d$ ,  $E_a$ , and  $E_d$  represent the direction cosines of the ascending ( $a$ ) and descending ( $d$ ) LOS vector and are estimated from the incidence angles ( $\alpha_a$  and  $\alpha_d$ ) and the LOS azimuths ( $\gamma_a$  and  $\gamma_d$ ) in degrees:

$$H_a = \cos(\alpha_a) \quad (3)$$

$$H_d = \cos(\alpha_d) \quad (4)$$

$$E_a = \cos(90 - \alpha_a) \times \cos(270 - \gamma_a) \quad (5)$$

$$E_d = \cos(90 - \alpha_d) \times \cos(270 - \gamma_d) \quad (6)$$

Figure 3 shows the SAR viewing geometry and the different parameters involved in the east and vertical components.

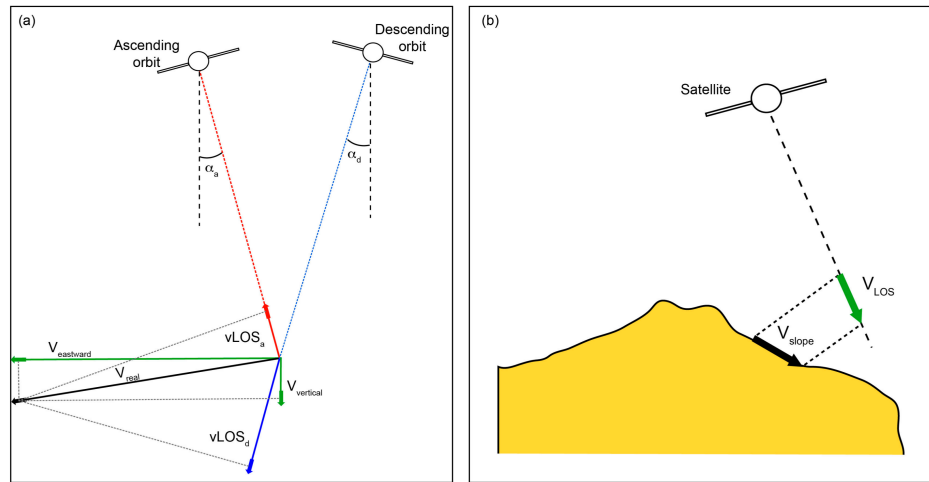


**Figure 3.** (a) Relationships between the incidence angles of the two viewing geometries (ascending and descending), the ground deformation rate ( $V_{real}$ ), the ascending and descending deformation rate ( $vLOS_a$  and  $vLOS_d$ ), and the east and vertical components of ground motion ( $V_{eastward}$  and  $V_{vertical}$ ); and (b) a schematic diagram showing the displacement rate along the LOS direction ( $vLOS$ ) and the projection of  $vLOS$  onto the direction of the maximum slope ( $V_{slope}$ ).

### 3.3. Projection of the LOS Deformation Rate onto the Maximum Slope Direction ( $V_{slope}$ )

In translational landslides the movement of the ground occurs mainly along the direction of the maximum slope and, therefore, the most representative component of the movement is considered to be the one parallel to this direction (e.g., [45]). In this case, a common strategy that can facilitate data interpretation is to project the LOS displacement onto the maximum slope direction ( $V_{slope}$ ) (e.g., [5,17,43]).

$V_{slope}$  can be estimated as the ratio between the displacement rate along the satellite LOS ( $vLOS$ ) and the percentage of the movement detected along the LOS ( $C$ ) of the coherent pixels located over the landslide body of both datasets (ascending and descending):

$$V_{slope} = vLOS/C \quad (7)$$

We estimate the coefficient  $C$  using the following equation [43]:

$$C = N \times (\cos(S) \times \sin(A - 90)) + E \times -1 \times (\cos(S) \times \cos(A - 90)) + H \times (\sin(S)) \quad (8)$$

where  $A$  and  $S$  are the aspect and the slope in degrees, derived from the digital elevation model;  $N$ ,  $E$ , and  $H$  represent the direction cosines of the LOS vector and are estimated from the incidence angle ( $\alpha$ ) and the LOS azimuth ( $\gamma$ ) in degrees, as:

$$N = \cos(90 - \alpha) \times \cos(180 - \gamma) \quad (9)$$

$$E = \cos(90 - \alpha) \times \cos(270 - \gamma) \quad (10)$$

$$H = \cos(\alpha) \quad (11)$$

Note that negative values of  $C$  represent movement of the ground towards the satellite. Some coherent pixels need to be removed before proceeding further to avoid the geometrical limitations of this type of projection [43]. We removed pixels located in local slopes with orientation different to main slope orientation (e.g., counter slope or small valley) and pixels with  $-0.2 < C < 0.2$  to avoid anomalous values of  $Vslope$ , due to exaggeration of the projection when  $C$  tends to zero (see [43]).  $Vslope$  is then calculated using Equation (3).

#### 3.4. Generating the Map of Vulnerable Buildings

We use a matrix-based approach, combining deformation and the severity of damages, to assign a vulnerability index to each building block. To jointly analyse building damage and ground deformation, we first assign a ground deformation rate value to each building block. For this evaluation, deformation along the most probable direction of displacement of the landslide was used [5]; this corresponds to the direction of maximum slope (i.e.,  $Vslope$ ), assuming a pure translational mechanism. To assign a  $Vslope$  value to each building, we first interpolate  $Vslope$  values using a nearest neighbour algorithm (with a quadrant search and 50 m search radius) and then we select the highest  $Vslope$  value inside the building block. We then separate between low and high building deformation rates, using the threshold of 1.6 cm/year, which is the threshold between extremely slow and very slow landslides [46]. Hence, building blocks with a deformation rate greater than 1.6 cm/year are referred to as urban hotspots.

During a field campaign carried out in March 2017, building damage in the La Verbena settlement was assessed and recorded following the scheme of Cooper [28]. This author rates the damage from 0 (no damage) to 7 (total collapse). Since the interiors of the buildings were not accessible, damage categories considered in the range from 2 (damages not visible from the outside) to 7 (total collapse). We inspected the region affected by the landslide and the neighbouring regions to constrain the affected area and discriminate damages produced by other phenomena. According to this work, the severity of damages affecting a building was classified into three values: low (buildings with damage category  $<3$ , i.e., no visible damages), moderate (buildings with damage category 3 or 4), and severe (buildings with damage category  $>4$ ).

Finally, for each building, we compare the value of the deformation rate with the damage category, and we assign a vulnerability index to the combination, following the scheme in Figure 4. The green, yellow, and red cells indicate low, medium, and high levels of vulnerability for buildings, based on the deformation rate threshold (vertical axis) and on the severity of damages according to Cooper scheme (horizontal axis). Low vulnerability indicates buildings with low deformation rates ( $<1.6$  cm/year) where no damage has been recorded ( $<3$ ). Medium vulnerability indicates buildings with low deformation rates where medium or high damage (buildings with damage category  $>2$ ) has been recorded. High vulnerability indicates buildings with high deformation rates, independently of the building damage. Buildings with no visible damages are included in this category because they could correspond to buildings where mitigation measures could prevent damage in the future.

		Building Damage level		
		Low (Cooper $<3$ )	Medium (Cooper 3,4)	High (Cooper $>4$ )
Building Deformation rate ( $Vslope$ )	Low ( $<1.6$ cm/yr)	Low	Medium	Medium
	High ( $\geq 1.6$ cm/yr)	High	High	High

**Figure 4.** Vulnerability matrix. Green, yellow, and red cells indicate low, medium, and high vulnerability building levels based on ratings of building deformation (vertical axis) and the severity of damages (horizontal axis).

## 4. Results

### 4.1. InSAR Results

Figure 5 shows the InSAR-derived maps of deformation rates for the study area from ascending and descending passes. These measurements indicate ground displacement along the satellite line-of-sight (LOS), which has an average value of  $44^\circ$  and  $38^\circ$  from vertical for ascending and descending geometries, respectively.

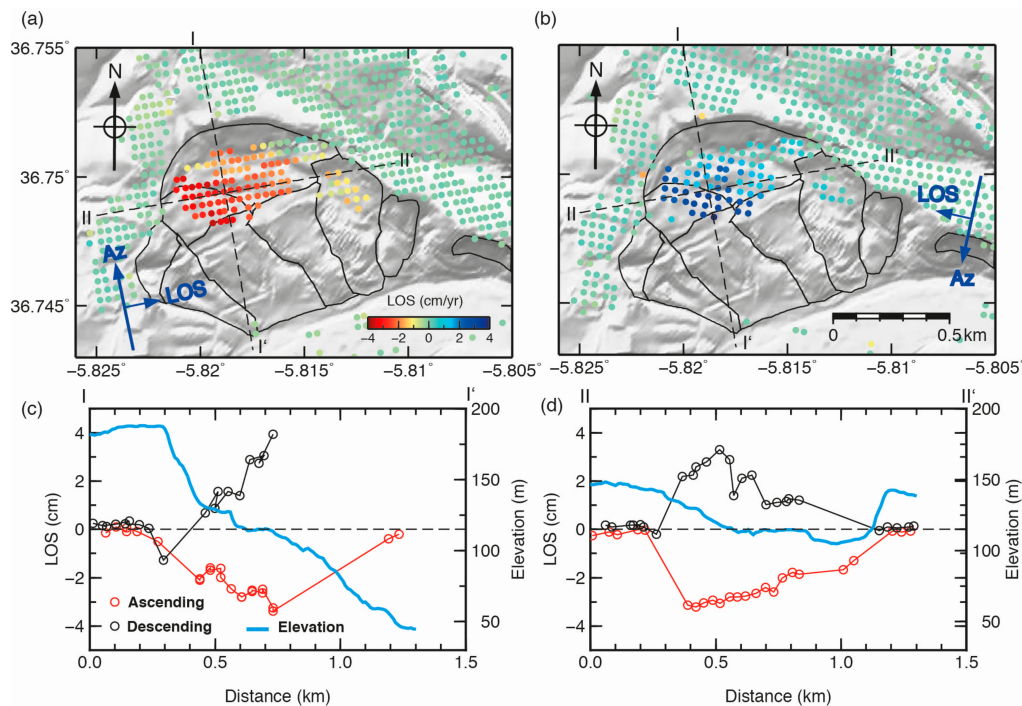


**Figure 5.** Deformation rate in the satellite LOS from ascending (a) and descending (b) orbits. The limits of the complex landslide are plotted as black lines. Black dashed lines show the location of cross-sections in (c) and (d). Blue arrows indicate satellite azimuth (Az) and line-of-sight direction (LOS). ((c) and (d)) Deformation rates along cross-sections I-I' and II-II' from ascending (red) and descending (black) passes. The blue line represents the elevation profile derived from the 25 m digital elevation model.

Both maps show a very similar deformation pattern, centred on the La Verbena settlement, with opposite signs: in the ascending map deformation values in La Verbena are negative and, thus, the ground moves away from the satellite, with maximum values of  $-3.6$  cm/year, while the descending deformation map shows positive values (ground towards the satellite) with maximum values of  $4.0$  cm/year. Note the striking symmetry of the deformation profiles in Figure 5c,d. This deformation pattern is consistent with the NNW-SSE movement of the Arcos de la Frontera landslide measured from ENVISAT data between April 2011 and May 2012 [46].

### 4.2. Horizontal and Vertical Deformation Rate

Figure 6 shows the eastward and vertical components of the landslide motion derived from the Sentinel-1 data. Eastward deformation reaches maximum values of  $5$  cm/year in the southern part of the La Verbena settlement, near the scarp of one of the landslides bodies. Vertical deformation rates show a pattern with maximum negative values of  $1$  cm/year (subsidence of the ground) along the crown area. This is consistent with a predominantly translational mechanism with a rotational component near the crown area. This behaviour is very frequent in planar slides, where a local rotation

in head takes place to accommodate curvature at the intersection of the basal surface and the back scarp [47].

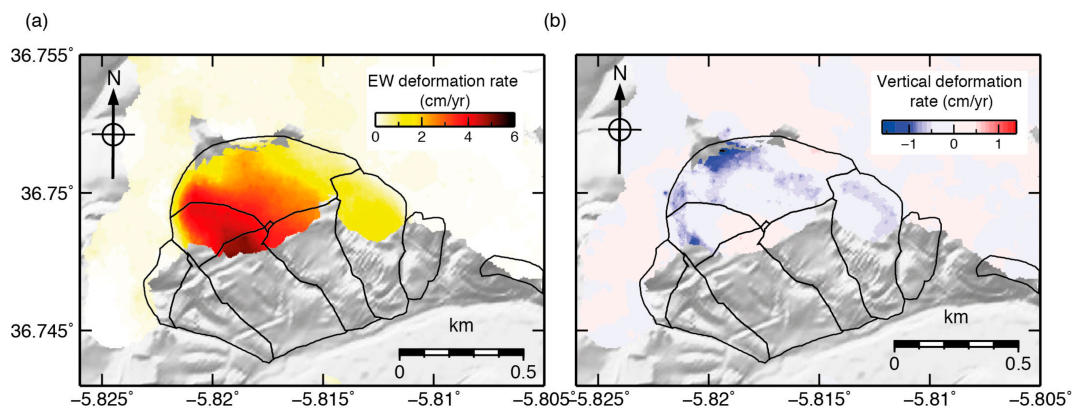


**Figure 6.** Deformation rate in the eastward (a) and vertical direction (b). The limits of the complex landslide are plotted as black lines

#### 4.3. Deformation Rates Projected onto the Maximum Slope Direction

Figure 7 shows the results of projecting LOS deformation rates along the maximum slope direction. Maximum deformation rates ( $\sim 10$  cm/year) are located in the centre and southwestern part of the La Verbena settlement, which is consistent with LOS velocities (Figure 5) and eastward velocities (Figure 6a). The points are heterogeneously distributed across La Verbena due to the filter applied to avoid anomalous values of  $V_{slope}$  due to local slopes with different orientations to the main slope and values of coefficient  $C$  close to 0 (see Section 3.3).

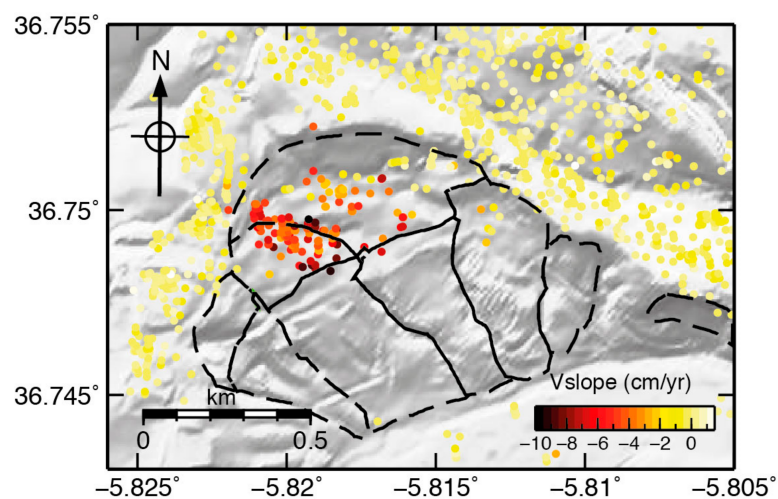


**Figure 7.** Deformation rate projected onto the maximum slope direction ( $V_{slope}$ ). The limits of the complex landslide are plotted as black lines.

#### 4.4. Classification of Buildings Damage

Most of the buildings in La Verbena show damages between categories 3 and 5 (Figure 8). The most affected areas (category 5: very severe) are located in the central part of the head of the landslide and in its eastern flank. Figure 9 shows some pictures of the most damaged areas taken in March 2017. The building block evacuated in 2009 is shown in Figure 9b.

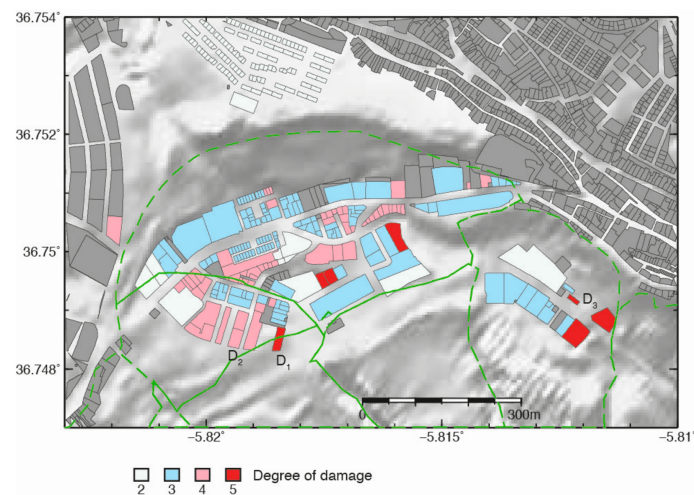


**Figure 8.** Building blocks classified using the damage classification scheme of Cooper [28]. Buildings where damages were not recorded are depicted in grey. The limits of the complex landslide are plotted as green dashed lines. Labels  $D_1$ ,  $D_2$ , and  $D_3$  indicate the location of buildings depicted in Figure 9.



**Figure 9.** (a) An opened joint in a building with damage category 4 (located at point labelled  $D_2$  in Figure 8); (b) a severely damaged building (damage category 5) evacuated in 2009 (located at point labelled  $D_1$  in Figure 8); and (c) a tilted building (damage category 5) located at point labelled  $D_3$  in Figure 8.

We also inspected the neighbourhoods adjacent to La Verbena searching for building damage:

- To the north of La Verbena, there is a neighbourhood built in 1970–1975 where no damage was visible and, thus, all buildings were assigned a degree of damage 2. This neighbourhood is very close to the crown area of the landslide, but it is located over a different, more stable material (calcarenites and sandstones, [48]).
- To the west of La Verbena there is an industrial park and a neighbourhood built in 2003–2006 with numerous buildings visibly damaged. We did not record in detail these damages because they are related to a different phenomenon: subsidence due to compaction of an artificial fill [44,49].
- To the east of La Verbena we found the old town. Although damage is visible in some historical buildings we did not record them because they are related to different phenomena that have affected the town in the past, such as the 1699 earthquake and the 1755 Lisbon earthquake, whose effects are visible in the tower of the Basilica Minor of Santa María de la Asunción (XIV Century) [50].

#### 4.5. Vulnerable Buildings Map

Figure 10 shows the deformation rate ( $V_{slope}$ ) assigned to each building block, the urban hotspots (i.e., building with deformation rate above the threshold of 1.6 cm/year) and the vulnerable buildings map.

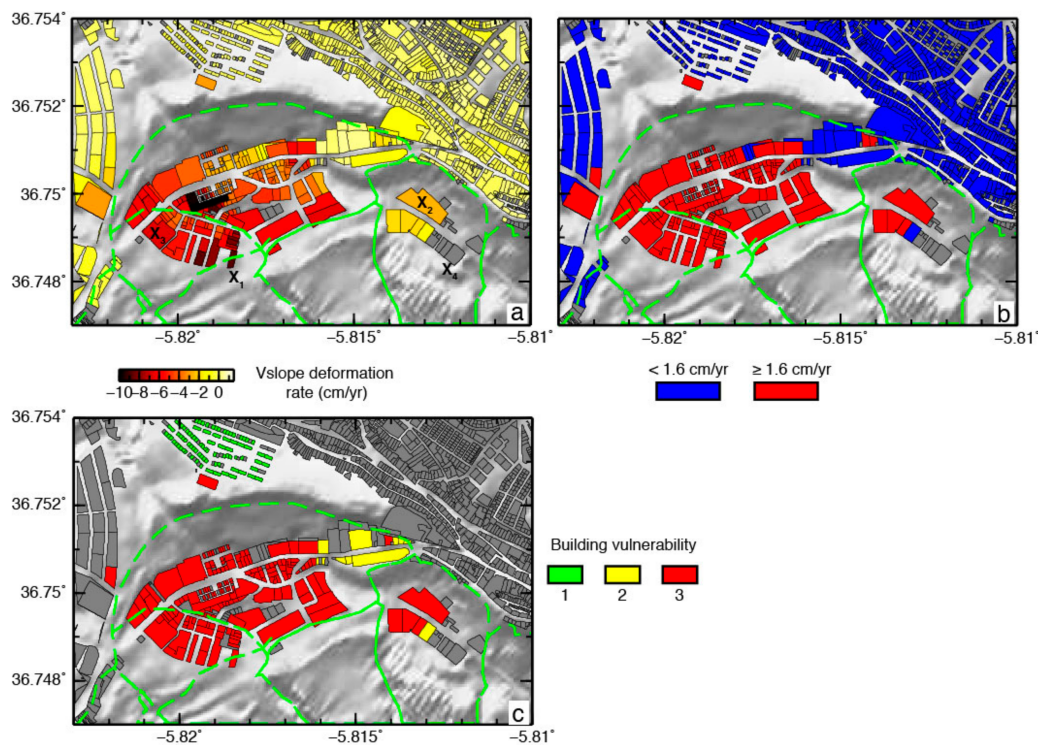


**Figure 10.** (a) Deformation rate projected onto the maximum slope direction ( $V_{slope}$ ) for each building block. Buildings where deformation rate could not be retrieved are depicted in grey.  $X_1$  indicates a building block with severe damages (category 5) and  $V_{slope}$  9 cm/year,  $X_2$  indicates a building block with no visible damages (category 2) and  $V_{slope}$  2 cm/year,  $X_3$  indicates a building block with no visible damages (category 2) and  $V_{slope}$  8 cm/year;  $X_4$  indicates a building where  $V_{slope}$  could not be estimated but  $vLOS$  could be retrieved (Supplementary Figure S2); (b) red buildings represent “deformation hotspots”, where  $V_{slope}$  is greater or equal to the threshold of 1.6 cm/year; and (c) building vulnerability.

Most of the buildings in La Verbena are hotspots and also some of the building close to the limits of the landslide. Inside La Verbena, some buildings show lower deformation rates, concentrated in the eastern limit of the landslide. The vulnerable buildings map (Figure 10c) shows the building blocks classified into the three classes of the vulnerability matrix (Figure 9). Most of the buildings in La Verbena present high vulnerability. Some buildings in the eastern part present medium vulnerability. The neighbourhood to the north has low vulnerability values, except for the building closest to the landslide limit (the southernmost one) which presents no visible damage, but high deformation rates.

## 5. Discussion

### 5.1. Geomorphology of the Landslide and Ground Deformation

InSAR-derived deformation estimated from Sentinel-1 SAR data has allowed us to identify an urban area in Arcos de la Frontera, South Spain that is currently suffering ground deformation associated to an active landslide. These results, combined with our geomorphological analysis (Figure 1b), permitted a redefinition of the landslide boundaries, which is composed of several bodies, most of them retrogressive, complex earthflow-earth slide, with a planar failure type.

The affected buildings are located near the crown of a landslide body. The deformation rate in La Verbena decreases from west to east (Figure 5d). This pattern seems to correlate with the boundaries of three landslides bodies (Figure 5a,b). This could indicate that the most active landslide body is that from the west and activity decreases eastward. This is consistent with geomorphology: while western

bodies present undulations, active cracks, a distorted and undeveloped drainage network, as well as many lobes revealing an intense soil creep, eastern bodies present a well-developed drainage network and hardly visible activity signs (Figure 1).

The estimation of the eastward and vertical component of the LOS deformation field allows us to characterize the mechanism of the landslide: most of the movement is horizontal (with maximum values of  $\sim 5$  cm/year) while the vertical movement is small (with maximum values of 1 cm/year) and concentrated near the crown area. This is consistent with a translational landslide type with some rotational components in the crown area.

### 5.2. Comparison of Damages Map and Deformation

In our case study, there is a clear spatial correlation between the landslide body, the ground deformation, and the location of damages (Figure 5a,b, Figure 7, and Figure 8). Ground deformation allows discriminating between areas affected by the landslide movement and stable areas. Overall, a good agreement is observed, for each building block, between the severity of building damage and the  $V_{slope}$  (Figure 11). Damaged buildings are located in areas with high deformation rates, and buildings with no visible damage have predominantly low deformation rates (less than 1.6 cm/year). However, some of these buildings are located in areas with deformation rates of more than 6 cm/year, and for buildings with damage category 3–4, we found both situations, with low and high deformation rates (Figure 11). To understand these results we must take into account that damage in this settlement due to the active landslides have been reported since 2006 and the ground deformation that we analysed is limited to the period 2015–2016. Therefore, buildings with no visible damage, but high deformation rates in this period, could correspond to areas where deformation began recently and, thus, its impact on buildings is not yet visible.

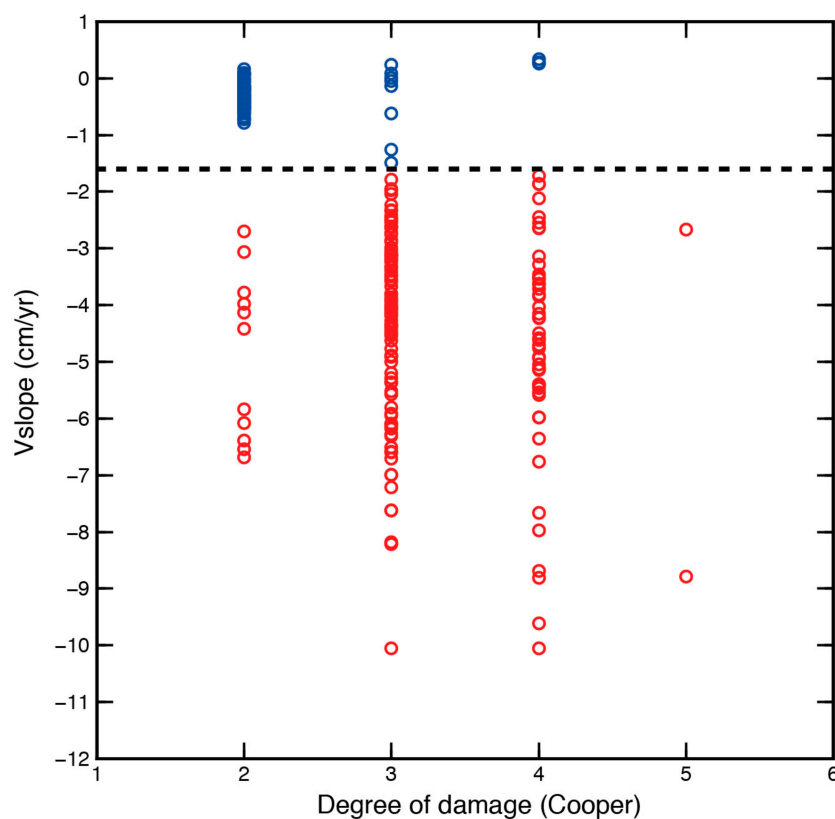


**Figure 11.** Deformation rate projected onto the maximum slope direction ( $V_{slope}$ ) versus the degree of damage for each building block. The horizontal black dashed line represents the  $V_{slope}$  threshold of 1.6 cm/year. Red points represent buildings where  $V_{slope}$  is greater or equal to this threshold.

Other factors not considered in our study that control building damage are the building construction date, the type of building and the type of foundation. Mateo et al. [25] reported heterogeneous building damages correlated with the type of housing (detached or terraced) and the quality of the foundations. Notti et al. [22] found a relationship between the severity of damage, the duration of ground deformation and the age of buildings. Bianchini et al. [21] concluded that building damage was mainly controlled by the combination of terrain morphology and the type of foundation that had been employed.

### 5.3. Vulnerable Buildings Map, Potential, and Limits

The vulnerable buildings map indicates that most of the building blocks in La Verbena present high vulnerability (93% of the building blocks where vulnerability could be estimated), suggesting that more in-depth local studies and mitigation measures should be applied globally to this settlement. It is worth noticing that buildings with high vulnerability (index 3) can refer to different situations: from severely damaged building (damage category 5) with high *Vslope* (9 cm/year), such as building labeled  $X_1$  in Figure 10a, to buildings with no visible damage (damage category 2) and *Vslope* slightly higher than the threshold of 1.6 cm/year (such as building labelled  $X_2$  in Figure 10a). The simplicity of this map meets the purpose of providing a quick product, easy for the non-expert user to understand. Additionally, the combination of this map with the map of buildings damage (Figure 8) and the map of deformation over buildings (Figure 10a) can be helpful to identify building blocks that require local in situ monitoring to evaluate the serviceability of each building [51–53]. For instance, it could be less urgent to perform local monitoring of building  $X_1$  in Figure 10a (already evacuated, with severe damages, Cooper 5, and high *Vslope*, 9 cm/year) than building  $X_3$  in Figure 10a, with no visible damages but high *Vslope* (8 cm/year), where the occurrence of severe damages in the future could be prevented and mitigated.

Other relevant information for managing authorities could be building deformation maps other than the *Vslope* map, so deformation affecting buildings where *Vslope* cannot be estimated (e.g., due to local slope orientation) can be evaluated. For example, for building labelled  $X_4$  in Figure 10a, no *Vslope* is available. However, the LOS deformation maps have a high density of coherent pixels around this building and then LOS deformation can be estimated (Supplementary Figure S2).

The methodology presented here allows us to generate maps of urban vulnerable areas affected by slow moving landslides as a support for local authorities, Civil Protection, and decision-makers. The strengths of this methodology are that the proposed products can be generated quickly and at low cost, since deformation is derived from free and open Sentinel-1 SAR data and building damage is recorded using a quick and easy-to-apply assessment method [28]. The map obtained is intended to support the selection of vulnerable urban areas where more in depth local studies should be applied to evaluate the building serviceability. Thanks to the continuous acquisition of Sentinel-1 SAR data every six days, these maps can be quickly generated after the disaster and regularly updated, which is fundamental to monitor the evolution of building deformation and the effectiveness of the mitigation measures.

This product is intended to be simple, but it can be combined with other information sources to create a more refined product. For instance, the use of high-resolution X-band data allows increasing the density of measurements over individual building, and might be of interest for other applications (e.g., estimation of differential settlements for each building, see [21,53]). Additionally, the information provided by our map can be completed by specifying the type of building evaluated (education centres, health facilities) following the requirements for damage and loss data sharing standard for the Sendai Framework for Disaster Risk Reduction [54]. Additionally, information about the construction date and foundation type for each building could considerably improve the vulnerable buildings map and its interpretation.

## 6. Conclusions

We have presented here a simple and fast methodology to generate maps of vulnerable building blocks, easily understandable to non-experts, aimed at helping local authorities, Civil Protection, and decision-makers manage the post-disaster situation in urban areas affected by slow-moving landslides. The methodology consists on the combination of two parameters: building damage and building deformation, and it is based on the assumption that the most vulnerable buildings are those with more severe damage and experiencing high deformation rates in the present.

We applied this methodology in La Verbena settlement (Arcos de la Frontera, South Spain), an urban area affected by an active landslide that has produced severe damage. Using Sentinel-1 images, we estimated the deformation rate associated to each building that was combined with the building damage generated by the landslide movement and recorded during a field campaign. The resulting vulnerable buildings map show that a 93% of the building blocks analysed in the settlement present high vulnerability and, thus, more in-depth local studies are necessary in order to evaluate the serviceability of the buildings of this area, prior to adopting the necessary mitigation measures that can help reduce the impact of this damaging landslide.

Thanks to the global availability of free and open Sentinel-1 SAR data, with continuous acquisitions every six days, this methodology can be applied to slow-moving landslides worldwide to quickly generate these maps after the disaster and regularly update them.

**Supplementary Materials:** The following are available online at [www.mdpi.com/2072-4292/9/9/876/s1](http://www.mdpi.com/2072-4292/9/9/876/s1), Figure S1. Orthoimages showing the evolution of the study area from 1956 to 2013; Figure S2. Building deformation estimated from ascending, descending, eastward, and vertical ground deformation rates.

**Acknowledgments:** This work is supported by the Spanish Ministry of Economy and Competitiveness and EU FEDER funds under projects ESP2013-47780-C2-2-R and ESP2013-47780-C2-1-R. Sentinel-1 data were provided by the European Space Agency (ESA). Some figures were prepared using the public domain GMT software (Wessel and Smith, 1998).

**Author Contributions:** M.B.-P., R.M.M., and G.H. designed the study. D.N. and P.E. processed InSAR data. G.C. and J.D. estimated the different components of ground deformation. M.B.-P., D.N., and G.B. recorded building damage and G.H. and R.M.M. mapped the landslide. M.B.-P., M.S., and L.S. created the vulnerable buildings map. All authors contributed to the analysis of the results. M.B.-P. and D.N. prepared the figures and wrote the manuscript with input from all team members.

**Conflicts of Interest:** The authors declare no conflict of interest.

## References

1. Petley, D. Global patterns of loss of life from landslides. *Geology* **2012**, *40*, 927–930. [[CrossRef](#)]
2. Haque, U.; Blum, P.; da Silva, P.F.; Haque, U.; Blum, P.; da Silva, P.F.; Andersen, P.; Pilz, J.; Chalov, S.R.; Malet, J.P.; et al. Fatal landslides in Europe. *Landslides* **2016**. [[CrossRef](#)]
3. Gariano, S.L.; Guzzetti, F. Landslides in a changing climate. *Earth-Sci. Rev.* **2016**, *162*, 227–252. [[CrossRef](#)]
4. Cruden, D.M. A simple definition of a landslide. *Bull. Int. Assoc. Eng. Geol.* **1991**, *43*, 27–29. [[CrossRef](#)]
5. Cigna, F.; Bianchini, S.; Casagli, N. How to assess landslide activity and intensity with Persistent Scatterer Interferometry (PSI): The PSI-based matrix approach. *Landslides* **2013**, *10*, 267–283. [[CrossRef](#)]
6. Calvello, M.; Peduto, D.; Arena, L. Combined use of statistical and DInSAR data analyses to define the state of activity of slow-moving landslides. *Landslides* **2017**, *14*, 473–489. [[CrossRef](#)]
7. Raspini, F.; Bardi, F.; Bianchini, S.; Ciampalini, A.; Del Ventisette, C.; Farina, P.; Ferrigno, F.; Solari, L.; Casagli, N. The contribution of satellite SAR-derived displacement measurements in landslide risk management practices. *Nat. Hazards* **2017**, *86*, 327–351. [[CrossRef](#)]
8. Scaioni, M.; Longoni, L.; Melillo, V.; Papini, M. Remote Sensing for Landslide Investigations: An Overview of Recent Achievements and Perspectives. *Remote Sens.* **2014**, *6*. [[CrossRef](#)]
9. Delacourt, C.; Allemand, P.; Casson, B.; Vadon, H. Velocity field of the “La Clapiere” landslide measured by the correlation of aerial and QuickBird satellite images. *Geophys. Res. Lett.* **2004**, *31*. [[CrossRef](#)]
10. Stumpf, A.; Malet, J.P.; Delacourt, C. Correlation of satellite image time-series for the detection and monitoring of slow-moving landslides. *Remote Sens. Environ.* **2017**, *189*, 40–55. [[CrossRef](#)]

11. Le Bivic, R.; Allemand, P.; Quiquerez, A.; Delacourt, C. Potential and Limitation of SPOT-5 Ortho-Image Correlation to Investigate the Cinematics of Landslides: The Example of “Mare à Poule d’Eau” (Réunion, France). *Remote Sens.* **2017**, *9*, 106. [[CrossRef](#)]
12. Raspini, F.; Ciampalini, A.; Del Conte, S.; Lombardi, L.; Nocentini, M.; Gigli, G.; Ferretti, A.; Casagli, N. Exploitation of Amplitude and Phase of Satellite SAR Images for Landslide Mapping: The Case of Montescaglioso (South Italy). *Remote Sens.* **2015**, *7*, 14576–14596. [[CrossRef](#)]
13. Singleton, A.; Li, Z.; Hoey, T.; Muller, J.-P. Evaluating sub-pixel offset techniques as an alternative to D-InSAR for monitoring episodic landslide movements in vegetated terrain. *Remote Sens. Environ.* **2014**, *147*, 133–144. [[CrossRef](#)]
14. Fruneau, B.; Achache, J.; Delacourt, C. Observation and model-ling of the Saint-Etienne-de-Tine’e landslide using SAR interferometry. *Tectonophysics* **1996**, *265*, 181–190. [[CrossRef](#)]
15. Colesanti, C.; Wasowski, J. Investigating landslides with space-borne Synthetic Aperture Radar (SAR) interferometry. *Eng. Geol.* **2006**, *88*, 173–199. [[CrossRef](#)]
16. Tofani, V.; Raspini, F.; Catani, F.; Casagli, N. Persistent Scatterer Interferometry (PSI) technique for landslide characterization and monitoring. *Remote Sens.* **2013**, *5*, 1045–1065. [[CrossRef](#)]
17. Herrera, G.; Gutiérrez, F.; García-Davalillo, J.C.; Guerrero, J.; Notti, D.; Galve, J.P.; Cooksley, G. Multi-sensor advanced DInSAR monitoring of very slow landslides: The Tena Valley case study (Central Spanish Pyrenees). *Remote Sens. Environ.* **2013**, *128*, 31–43. [[CrossRef](#)]
18. Massonnet, D.; Feigl, K.L. Radar interferometry and its application to changes in the Earth’s surface. *Rev. Geophys.* **1998**, *36*, 441–500. [[CrossRef](#)]
19. Herrera, G.; Notti, D.; García-Davalillo, J.C.; Mora, O.; Cooksley, G.; Sánchez, M.; Arnaud, A.; Crosetto, M. Analysis with C- and X-band satellite SAR data of the Portalet landslide area. *Landslides* **2011**, *8*, 195–206. [[CrossRef](#)]
20. Bardi, F.; Frodella, W.; Ciampalini, A.; Bianchini, S.; Del Ventisette, C.; Gigli, G.; Fanti, R.; Moretti, S.; Basile, G.; Casagli, N. Integration between ground based and satellite SAR data in landslide mapping: The San Fratello case study. *Geomorphology* **2014**, *223*, 45–60. [[CrossRef](#)]
21. Bianchini, S.; Pratesi, F.; Nolesini, T.; Casagli, N. Building Deformation Assessment by Means of Persistent Scatterer Interferometry Analysis on a Landslide-Affected Area: The Volterra (Italy) Case Study. *Remote Sens.* **2015**, 4678–4701. [[CrossRef](#)]
22. Notti, D.; Galve, J.P.; Mateos, R.M.; Montserrat, O.; Lamas-Fernández, F.; Fernández-Chacón, F.; Roldán-García, F.J.; Pérez-Peña, V.; Crosetto, M.; Azañón, J.M. Human-induced coastal landslide reactivation. Monitoring by PSInSAR techniques and urban damage survey (SE Spain). *Landslides* **2015**, *12*, 1007–1014. [[CrossRef](#)]
23. Cascini, L.; Peduto, D.; Pisciotta, G.; Arena, L.; Ferlisi, S.; Fornaro, G. The combination of DInSAR and facility damage data for the updating of slow-moving landslide inventory maps at medium scale. *Nat. Hazards Earth Syst. Sci.* **2013**, *13*, 1527–1549. [[CrossRef](#)]
24. Ciampalini, A.; Bardi, F.; Bianchini, S.; Frodella, W.; Ventisette, C.D.; Moretti, S.; Casagli, N. Analysis of building deformation in landslide area using multisensor PSInSARTM technique. *Int. J. Appl. Earth Obs. Geoinf.* **2014**. [[CrossRef](#)] [[PubMed](#)]
25. Mateos, R.M.; Azañón, J.M.; Roldán, F.J.; Notti, D.; Pérez-Peña, V.; Galve, J.P.; Pérez-García, J.L.; Colomo, C.M.; Gómez-López, J.M.; Montserrat, O.; et al. The combined use of PSInSAR and UAV photogrammetry techniques for the analysis of the kinematics of a coastal landslide affecting an urban area (SE Spain). *Landslides* **2017**, *14*, 743–754. [[CrossRef](#)]
26. Infante, D.; Confuorto, P.; Di Martire, D.; Ramondini, M.; Calcaterra, D. Use of DInSAR Data for Multi-level Vulnerability Assessment of Urban Settings Affected by Slow-moving and Intermittent Landslides. *Procedia Eng.* **2016**, *158*, 470–475. [[CrossRef](#)]
27. Peduto, D.; Nicodemo, G.; Maccabiani, J.; Ferlisi, S. Multi-scale analysis of settlement-induced building damage using damage surveys and DInSAR data: A case study in The Netherlands. *Eng. Geol.* **2017**, *218*, 117–133. [[CrossRef](#)]
28. Cooper, A.H. The classification, recording, databasing and use of information about building damage caused by subsidence and landslides. *Q. J. Eng. Geol. Hydrogeol.* **2008**, *41*, 409–424. [[CrossRef](#)]
29. Sanz de Galdeano, C.; Vera, J.A. Una propuesta de clasificación de las cuencas neógenas béticas. *Acta Geológica Hispánica* **1991**, *26*, 205–227. (In Spanish)

30. Tsige, M.; González de Vallejo, L.; Doval, M.; Barba, C. Microfabric of Guadalquivir “Blue Marls” and its engineering geological significance. In Proceedings of the 7th International IAEG Congress, Lisboa, Portugal, 5–9 September 1994; Volume 4, pp. 45–51.
31. Alonso, E.E.; Pinyol, N.M.; Puzrin, A.M. Earth Dam Sliding Failure: Aznalcóllar Dam. Spain. In *Geomechanics of Failures. Advanced Topics*; Springer International Publishing: Berlin, Germany, 2010; pp. 129–167.
32. Oteo, C. Las Margas Azules del Guadalquivir y la Inestabilidad de Taludes. *Rev. Rutas* **2000**, *77*, 17–27. (In Spanish)
33. Mancheño, M. *Apuntes para una historia de Arcos de la Frontera*; Tipografía Arcobricense: Cádiz, Spain, 1894. (In Spanish)
34. García, A. *Apuntes para una historia de Arcos de la Frontera. Término municipal de Arcos de la Frontera (Cádiz)*; Technical Report; Servicio Geológico de Obras Públicas: Madrid, Spain, 1970; unpublished. (In Spanish)
35. El País. Available online: [https://politica.elpais.com/politica/2017/03/04/actualidad/1488631296\\_954971.html](https://politica.elpais.com/politica/2017/03/04/actualidad/1488631296_954971.html) (accessed on 22 July 2017).
36. Granada Hoy. Available online: [http://www.granadahoy.com/andalucia/Arcos-ciudad-agrietada-desliza\\_0\\_458654602.html](http://www.granadahoy.com/andalucia/Arcos-ciudad-agrietada-desliza_0_458654602.html) (accessed on 22 July 2017).
37. Junta de Andalucía, Orthoimages Covering the Andalusian Region. Available online: [http://www.juntadeandalucia.es/medioambiente/site/rediam/menuitem.aedc2250f6db83cf8ca78ca731525ea0/?vgnnextoid=867122ad8470f210VgnVCM1000001325e50aRCRD&lr=lang\\_es](http://www.juntadeandalucia.es/medioambiente/site/rediam/menuitem.aedc2250f6db83cf8ca78ca731525ea0/?vgnnextoid=867122ad8470f210VgnVCM1000001325e50aRCRD&lr=lang_es) (accessed on 19 July 2017).
38. Mora, O.; Mallorquí, J.J.; Broquetas, A. Linear and nonlinear terrain deformation maps from a reduced set of interferometric SAR images. *IEEE Trans. Geosci. Remote Sens.* **2003**, *41*, 2243–2253. [[CrossRef](#)]
39. Blanco-Sánchez, J.; Mallorquí, J.; Duque, S.; Monells, D. The Coherent Pixels Technique (CPT): An Advanced DInSAR Technique for Nonlinear Deformation Monitoring. *Pure Appl. Geophys.* **2008**, *165*, 1167–1193. [[CrossRef](#)]
40. Confuorto, P.; Di Martire, D.; Centolanza, G.; Iglesias, R.; Mallorquí, J.J.; Novellino, A.; Plank, S.; Ramondini, M.; Thuro, K.; Calcaterra, D. Post-failure evolution analysis of a rainfall-triggered landslide by multi-temporal interferometry SAR approaches integrated with geotechnical analysis. *Remote Sens. Environ.* **2017**, *188*, 51–72. [[CrossRef](#)]
41. Centolanza, G.; Duro, J.; Mallorquí, J.J. Achieving precise Sentinel 1 coregistration with CPT, experience and lesson learnt. In Proceedings of the Fringe 2017 Workshop, Helsinki, Finland, 5–9 June 2017.
42. Raspini, F.; Cigna, F.; Moretti, S. Multi-Temporal Mapping of Land Subsidence at Basin Scale Exploiting Persistent Scatterer Interferometry: Case Study of Gioia Tauro Plain (Italy). *J. Maps* **2012**. [[CrossRef](#)]
43. Notti, D.; Herrera, G.; Bianchini, S.; Meisina, C.; García-Davalillo, J.C.; Zucca, F. A methodology for improving landslide PSI data analysis. *Int. J. Remote Sens.* **2014**, *35*, 2186–2214.
44. Bru, G.; González, P.J.; Mateos, R.M.; Roldán, F.J.; Herrera, G.; Béjar-Pizarro, M.; Fernández, J. A-DInSAR monitoring of landslide and subsidence activity: A Case of Urban Damage in Arcos de la Frontera, Spain. *Remote Sens.* **2017**, *9*, 787. [[CrossRef](#)]
45. Meisina, C.; Zucca, F.; Notti, D.; Colombo, A.; Cucchi, A.; Savio, G.; Giannico, C.; Bianchi, M. Geological interpretation of PSInSAR data at regional scale. *Sensors* **2008**, *8*, 7469–7492. [[CrossRef](#)] [[PubMed](#)]
46. Cruden, D.M.; Varnes, D.J. Landslide types and processes. In *Landslides: Investigation and Mitigation*; Turner, A.K., Schuster, R.L., Eds.; Transportation Research Board, National Research Council, National Academy Press: Washington, DC, USA, 1996; pp. 36–75.
47. Hutchinson, J.N. General Report: Morphological and geotechnical parameters of landslides in relation to geology and hydrogeology. In Proceedings of the 5th International Symposium on Landslides, Lausanne, Switzerland, 10–15 July 1988; Volume 1, pp. 3–25.
48. Jerez, L.; Moreno, E.; Granados, L.F.; Leyva, F. Geological Map of Spain, region 1049 (Arcos de la Frontera). Technical Report. IGME 1990. (In Spanish) Available online: [http://info.igme.es/cartografiadigital/geologica/Magna50Hoja.aspx?Id=1049#memoria\\_y\\_metadatos](http://info.igme.es/cartografiadigital/geologica/Magna50Hoja.aspx?Id=1049#memoria_y_metadatos) (accessed on 21 August 2017).
49. Santos, J. Obras reales y recalces en arcillas expansivas y suelos colapsables. In *1ª Jornada Sobre Ingeniería del Terreno*; Universidad de Jaén: Jaén, Spain, 2010. (In Spanish)
50. Martínez-Solares, J.M. *Los Efectos en España del Terremoto de Lisboa (1 de Noviembre de 1755)*; Dirección General del Instituto Geográfico Nacional: Madrid, Spain, 2001. (In Spanish)

51. Herrera, G.; Álvarez Fernández, M.I.; Tomás, R.; González-Nicieza, C.; Lopez-Sanchez, J.M.; Álvarez Vigil, A.E. Forensic analysis of buildings affected by mining subsidence based on Differential Interferometry (Part III). *Eng. Fail. Anal.* **2012**, *24*, 67–76. [[CrossRef](#)]
52. Tomás, R.; García-Barba, J.; Cano, M.; Sanabria, M.P.; Ivorra, S.; Duro, J.; Herrera, G. Subsidence damage assessment of a gothic church using Differential Interferometry and field data. *Struct. Health Monit.* **2012**, *11*, 751–762. [[CrossRef](#)]
53. Sanabria, M.P.; Guardiola-Albert, C.; Tomás, R.; Herrera, G.; Prieto, A.; Sánchez, H.; Tessitore, S. Subsidence activity maps derived from DInSAR data: Orihuela case study. *Nat. Hazards Earth Sci. Syst.* **2014**, *14*, 1341–1360. [[CrossRef](#)]
54. Corbane, C.; De Groeve, T.; Ehlich, D. *Guidance for Recording and Sharing Disaster Damage and Loss Data: Towards the Development of Operational Indicators to Translate the Sendai Framework into Action*; EU expert working group on disaster damage and loss data (2015), Publications Office of the European Union: Luxembourg City, Luxembourg, 2015; ISBN 978-92-79-47452-1. [[CrossRef](#)]



© 2017 by the authors. Licensee MDPI, Basel, Switzerland. This article is an open access article distributed under the terms and conditions of the Creative Commons Attribution (CC BY) license (<http://creativecommons.org/licenses/by/4.0/>).